This is an open access article published under a Creative Commons Non-Commercial No Derivative Works (CC-BY-NC-ND) Attribution License, which permits copying and redistribution of the article, and creation of adaptations, all for non-commercial purposes.

ACS AUTHORCHOICE

ACS APPLIED ELECTRONIC MATERIALS

Article

Cite This: ACS Appl. Electron. Mater. 2019, 1, 2585−2593

pubs.acs.org/acsaelm

Direct Epitaxial Growth of Polar $(1 - x)HfO_2-(x)ZrO_2$ Ultrathin Films on Silicon

Pavan Nukala,*[,†,∥] Jordi Antoja-Lleonart,[†,∥] Yingfen Wei,[†] Lluis Yedra,[‡,§] Brahim Dkhil,[‡] and Beatriz Noheda*[,†]

[†]Zernike Institute of Advanced Materials, University of Groningen, Groningen 9747 AG, The Netherlands

[‡]Laboratoire Structures, Propriétés et Modélisation des Solides, CentraleSupélec, CNRS UMR 8580, Université Paris-Saclay, 91190 Gif-sur-Yvette, France

[§]Laboratoire Mécanique des Sols, Structures et Matériaux, CentraleSupélec, CNRS UMR 8579, Université Paris-Saclay, 91190 Gif-sur-Yvette, France

Supporting Information

ABSTRACT: Ultrathin $Hf_{1-x}Zr_xO_2$ films have attracted tremendous interest since they show ferroelectric behavior at the nanoscale, where other ferroelectrics fail to stabilize the polar state. Their promise to revolutionize the electronics landscape comes from the well-known Si compatibility of HfO_2 and ZrO_2, which (in amorphous form) are already used as gate oxides in MOSFETs. However, the recently discovered crystalline ferroelectric phases of hafnia-based films have been grown on Si only in polycrystalline form. Better ferroelectric properties and improved quality of the interfaces have been achieved in epitaxially grown films, but these are only obtained on non-Si and buffered Si(100) substrates. Here, we report direct epitaxy of polar $Hf_{1-x}Zr_xO_2$ phases on Si, enabled via *in situ* scavenging of the native a-SiO_x layer by Zr (Hf), using pulsed laser deposition under ballistic deposition conditions. We investigate the effect of substrate orientation and film composition to provide fundamental insights into the conditions that lead to the preferential stabilization of polar phases, namely, the rhombohedral (r-) and the orthorhombic (o-) phases, against the nonpolar monoclinic (m-), on Si.

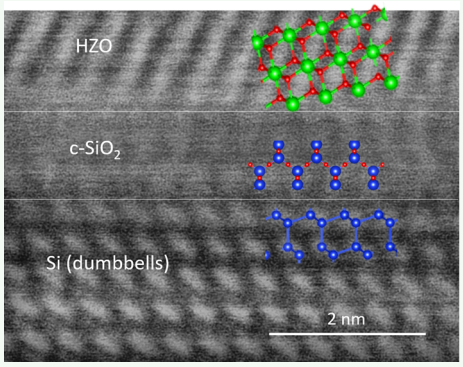

KEYWORDS: *Si-epitaxy, ferroelectric hafnia, polar rhombohedral phase, polar orthorhombic phase, native oxide scavenging*

INTRODUCTION

Ferroelectric hafnia-based thin films[1] have by now been established as the most promising materials to realize the potential of ferroelectric phenomena in real devices.[2,3] Their Si compatibility, simple chemistry, and unique ferroelectricity, which becomes more robust with miniaturization, is tailor-made for microelectronics, offering ready-made alternatives to conventional ferroelectrics that lack all these attributes.[4−12] Such distinguishing characteristics led to an upsurge in application-oriented research as well as in curiosity-driven fundamental research to solve questions such as why these materials are capable of sustaining the unconventional ferroelectricity,[13,14,23−32,15−22] how these materials negate the effects of depolarization fields,[33,34] and whether such a new type of ferroelectricity can be replicated in other simple oxide systems.

A prominent feature of hafnia-based materials is polymorphism.[35] While the ground state in the bulk HfO_2 is a nonpolar monoclinic (m-, $P2_1/c$) phase, a plethora of low-volume both polar and nonpolar metastable states can be stabilized at ambient conditions via a combination of strategies such as cationic and anionic doping,[1,15−17,19,22] thermal and inhomogeneous stresses,[36,37] nanostructuring,[38] epitaxial strain,[16,19,24,28,30,31,39−42] and oxygen vacancy engineering,[43,44] all of which can be suitably engineered into thin-film geometries. Based on first-principles calculations[23,39,45,46] at least five polar polymorphs (with space groups $Pca2_1$, Cc, $Pmn2_1$, $R3$, and $R3m$) can be identified as those that can be experimentally obtained. Owing to its relatively low energy, the orthorhombic (o-) $Pca2_1$ phase is widely observed in hafnia-based films grown via atomic layer deposition (ALD),[1,15,25,32] chemical solution deposition (CSD),[18] RF sputtering on Si,[26,29] and pulsed-laser deposition (PLD) on selected substrates.[16,21,27,31,40−42] A slightly higher energy rhombohedral (r-) phase ($R3m$ or $R3$) has been recently observed on epitaxial $Hf_{1/2}Zr_{1/2}O_2$ films grown on $SrTiO_3$ (STO).[39] The r-phase is stabilized by a combination of the large surface energy induced internal pressure of the nanoparticles and the substrate-imposed compressive strain. The epitaxial growth of the r-phase enabled the observation of the highest values of

Received: September 9, 2019
Accepted: November 23, 2019
Published: November 25, 2019

 © 2019 American Chemical Society

DOI: 10.1021/acsaelm.9b00585
ACS Appl. Electron. Mater. 2019, 1, 2585−2593

Table 1. Calculated 2θ Values for Different Bragg Spots as They Are Expected in Monoclinic, Rhombohedral, and Orthorhombic HZO

2θ (deg)	200	020	002	111	$\bar{1}11$	$1\bar{1}1$	$11\bar{1}$
monoclinic	35.47	34.98	34.37	28.49	31.71	28.49	31.71
rhombohedral	35.15	35.15	35.15	30.26	30.33	30.33	30.33
orthorhombic	35.82	34.20	35.09	30.23	30.23	30.23	30.23

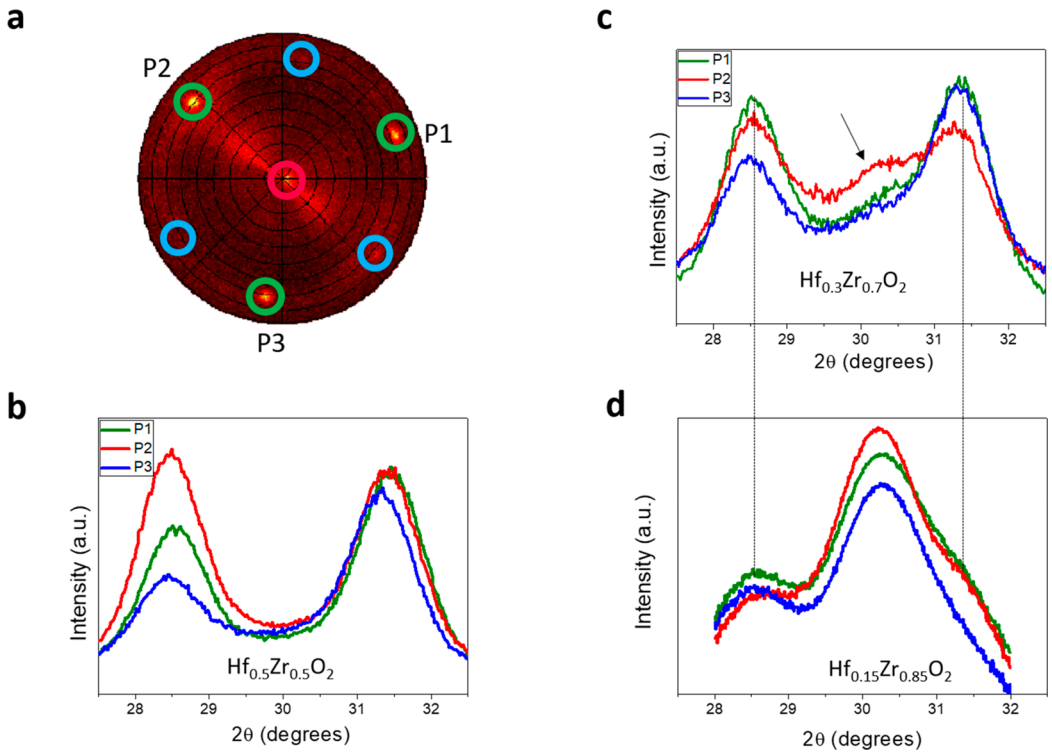

Figure 1. Texture and phase analysis on 10 nm $(1 - x)HfO_2$:$xZrO_2$ films (t = 10 nm) grown on Si(111). (a) Representative pole figure obtained at about $2\theta = 30°$ on film with $x = 0.7$, consistent with ⟨111⟩ out-of-plane texture. The three non-out-of-plane {111} poles, P1−P3, arising out of the film are centered at $\chi \approx 71°$ and separated in φ by 120°. These are highlighted with green circles in the figure. Rotated 180° from the film pattern, we see weak spots arising from the tail of substrate non-out-of-plane {111} poles at $2\theta = 28.44°$, this time highlighted with blue circles. Pole figure symmetry looks similar for $x = 0.5$ and $x = 0.85$ (Figure S1). θ−2θ scans around P1, P2, and P3 for x = (b) 0.5, (c) 0.7, and (d) 0.85. While (b) x = 0.5 shows just the monoclinic {111} peaks, a low-volume phase peak starts evolving from (c) $x = 0.7$ at $2\theta \approx 30.2°$ and intensifies at (d) $x = 0.85$.

spontaneous polarization (P_s = 34 $\mu C/cm^2$) in HfO_2−ZrO_2 systems, although they showed larger coercive fields than films in the polar o-phase.

So far, polar phases have been successfully obtained via epitaxial synthesis techniques (PLD) on a variety of substrates: perovskites[24,40−42] (including buffered STO on Si (001)),[42] fluorites,[16,27,31] and hexagonal substrates.[47] However, the advantages gained by epitaxy are offset by the fact that none of these films are grown directly on Si, despite the Si integrability of hafnia-based systems. It is in this context that we explore for the first time the epitaxy of polar polymorphs in $(1 - x)HfO_2$−$xZrO_2$ (HZO (x)) films directly on Si.

Direct epitaxial growth of oxides on Si is complicated by the presence of a very thin amorphous native oxide layer, which prevents the transfer of texture from the substrate to the film. This interfacial layer can be removed prior to deposition through hydrofluoric (acid etching), which lowers the crystalline quality.[48,49] However, the epitaxial growth of yttria-stabilized zirconia (YSZ) on Si(100) is a mature process,[50−53] as witnessed by the fact that YSZ-buffered Si(100) substrates are commonly used for the growth of high-T_c superconductors and other functional layers.[54−58] The problem of native oxide in YSZ on Si is solved via an *in situ* scavenging process. Since the formation energy of ZrO_2 (Y_2O_3) is less than that of SiO_2, Zr (Y) chemically reacts with a-SiO_2, forming a crystalline seed of ZrO_2(Y_2O_3) directly on Si, with an epitaxial relation.[49,56,59] In other words, the scavenging process involves one (or both) of the following decomposition chemical reactions.

$$SiO_2 + Zr \rightarrow Si + ZrO_2 \quad (1)$$

$$2SiO_2 + Zr \rightarrow ZrO_2 + 2SiO\uparrow \quad (2)$$

As a consequence of this scavenging process, the native SiO_x layer is replaced by ZrO_2 (Y_2O_3). The rest of the YSZ growth follows the template set by the crystalline ZrO_2 seed, formed as a result of scavenging the native amorphous oxide, resulting in a very high crystalline quality. The regrowth of the a-SiO_2 oxide (backward reactions 1 and 2, upon increasing the amount of product) and generation of misfit dislocations contribute to strain-relaxation in thicker layers of YSZ. Inspired by the success of direct epitaxy of a sister compound YSZ on Si, here, we report successful growth of epitaxial polar phases of HfO_2−ZrO_2 alloys directly on Si(111) and Si(100).

DOI: 10.1021/acsaelm.9b00585
ACS Appl. Electron. Mater. 2019, 1, 2585−2593

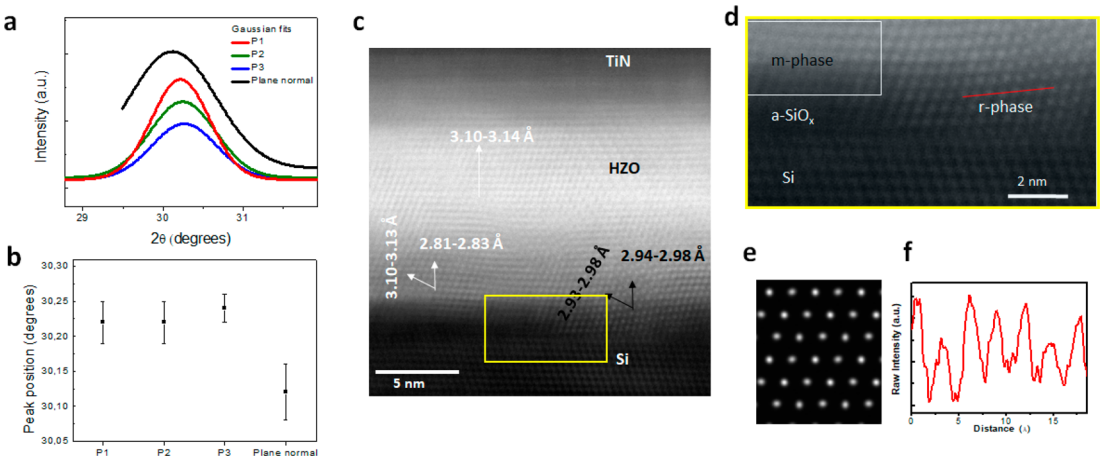

Figure 2. Determination of symmetry for the low-volume phase on Si(111). (a) Gaussian fits for the non-out-of-plane {111} poles P1−P3 and the plane normal (out-of-plane) corresponding exclusively to the low-volume phase for films with $x = 0.85$ ($t = 10$ nm). The raw data (Figure 1d) and 3-peak fitting procedure (two monoclinic, and one low-volume phase) are shown in Figure S1b. (b) Peak positions of the P1−P3 compared to the plane normal obtained from part a. This clearly reveals a 3:1 degeneracy in peak positions, or an r-phase. Error estimation is shown in Figure S2. The r-phase is further corroborated from $\theta-2\theta$ scans at the {001} poles shown in Figure S3. (c) Cross-sectional HAADF-STEM image of TiN−HZO ($x = 0.7$, $t = 10$ nm)-Si MIS capacitor (obtained along the $\langle 1\bar{1}0\rangle$ zone of the substrate), showing various {111} d-spacings. $d_{\{11\bar{1}\}} = 2.81 \pm 0.02$ Å, and $d_{\{111\}} = 3.11 \pm 0.02$ Å are quite clearly bulk m-phase parameters. The low-volume phase becomes a suspect when $d_{\{111\}}$ values are measured between 2.90 and 3.00 Å. (d) Zoomed-in look at the Si−HZO interface, boxed in yellow in part c. The interface with Si on the left contains regrown a-SiO_x (<1 nm). We clearly see an m-phase right above it. The region on the right has no a-SiO_x, but instead a direct connection between HZO and the crystalline substrate. That is a low-volume phase. (e) $R3$ phase HAADF-STEM multislice image simulation at lamella thickness of ∼20 nm (defocus ∼0). This corresponds rather well to our image. In particular the contrast fluctuations along the red line ($\langle 112\rangle$ direction) in part d are shown in part f, do not appear in the o- or t-phase, and are quite unique to the r-phases (as can be seen visually in part e).

EXPERIMENTAL METHODS

PLD was used for the deposition of HZO (x) with $x = 0.5$, 0.7, and 0.85 on p-doped Si(111) (resistivity <0.005 Ω cm), and Si(100) (resistivity <0.03 Ω cm). Targets of the desired compositions ($x = 0.5$, 0.7, 0.85) were prepared through standard solid-state synthesis starting from powders of HfO_2 (99% purity) and ZrO_2 (99.5% purity). A KrF excimer laser ($\lambda = 248$ nm) was used for target ablation at a fluence of 1.1 J/cm^2. A base pressure of 10^{-7} Torr was maintained in the deposition chamber. Target to substrate distance was fixed at 50 mm. HZO layers were deposited at 800 °C with the flow of Ar carrier gas (5 sccm) at a process pressure of 0.005 mbar and laser repetition rate of 7 Hz.

The choice of target−substrate distance, as well as the low pressure conditions, ensured a ballistic mode of deposition, preventing the oxidation of atomic species (Hf, Zr ions) in the plasma itself. It is indeed crucial for the interfacial scavenging reactions that species transported to the substrate are Hf, Zr, and O ions with no ionized HfO_2 and ZrO_2 present in the plasma. The 7 Hz repetition rate favors nucleation-dominated kinetics or, in this case, the occurrence of interfacial scavenging at multiple locations, and thus the generation of several (Hf)ZrO_2 seeds or growth templates.

On Si(111), HZO (x) films of 10 nm thickness with three different compositions ($x = 0.5$, 0.7, 0.85) were deposited, at a growth rate of 0.7 Å/s. On Si(100), films of 5, 10, and 20 nm were deposited with composition $x = 0.7$, at a growth rate of 0.9 Å/s. Thickness was confirmed from both scanning transmission electron microscopy (STEM) and X-ray reflectivity measurements. Information about global structure, symmetry, phase-mixing, and domains was inferred from X-ray diffraction (XRD) with a Cu Kα source. Texture analysis was performed via $\chi-\varphi$ (pole figure) scans at $2\theta \approx 30.0°$ (approximately corresponding to the $d_{\{111\}}$ of the low-volume phases) and at $2\theta \approx 34.5°$ (approximately corresponding to the $d_{\{200\}}$ of all the polymorphs). Table 1 provides the 2θ values that are expected of some of the relevant low-index planes in the three main HZO phases discussed in this work. The d-spacings of the poles obtained from the $\chi-\varphi$ equal area projections were more precisely analyzed through $\theta-2\theta$ scans around them.

Local structural characterization and phase analysis was performed through STEM imaging at 200 kV (Titan G2 and Themis). STEM images were obtained in both high-angle annular dark field (HAADF) mode, and bright-field (BF) mode. Chemical maps were generated via energy dispersive spectroscopy (EDS) in a four-detector ChemiSTEM setup on the Titan G2 aberration-corrected electron microscope.

RESULTS AND DISCUSSION

$(1 - x)HfO_2-xZrO_2$ on Si(111). *Strongly Textured (111) Films.* Pole figures obtained from films with $x = 0.5$, 0.7 (Figure 1a), and 0.85 (Figure S1a) at about $2\theta = 30.0°$ look qualitatively similar. In addition to the peak at the center (out-of-plane), there are three poles (P1−P3) arising from the film at $\chi \sim 71°$ separated from each other in φ by ∼120°. The weaker poles at $\chi \sim 71°$ (Figure 1a) are from the tail of the substrate peak at $2\theta = 28.44°$. This symmetry is consistent with $\langle 111\rangle$-oriented films, following the substrate. Quite interestingly, the {111} poles corresponding to the substrate and the film are rotated 180° about the substrate normal.

Phase Coexistence and Evidence of r-Phase. On the films with $x = 0.5$, the $\theta-2\theta$ scans across P1−P3 clearly show two peaks at every pole centered with $2\theta = 28.5°$ and 31.4° (Figure 1b), corresponding to $d_{\{111\}}$ and $d_{\{11\bar{1}\}}$ of the bulk m-phase. With the increase of Zr concentration to $x = 0.7$ (arrow in Figure 1c), a peak corresponding to a low-volume phase starts to appear at $2\theta = 30.23°$, with the majority phase still being monoclinic. A further increase in Zr concentration changes the predominant phase of the film to this low-volume phase, with a very minor fraction in the m-phase (Figure 1d). To determine the symmetry of the low-volume phase for the films with $x = 0.85$, a three-peak Gaussian fitting was performed to the $\theta-2\theta$ plots from P1, P2, and P3 between 2θ of 27° and 33° (Figure S1b,c). The peak position representing the low-volume phase is at $2\theta = 30.24 \pm 0.03°$ for P1, P2, and P3 whereas the out-of-plane peak is at $2\theta = 30.12 \pm 0.04°$ (see Figure 2a,b and

DOI: 10.1021/acsaelm.9b00585
ACS Appl. Electron. Mater. 2019, 1, 2585−2593

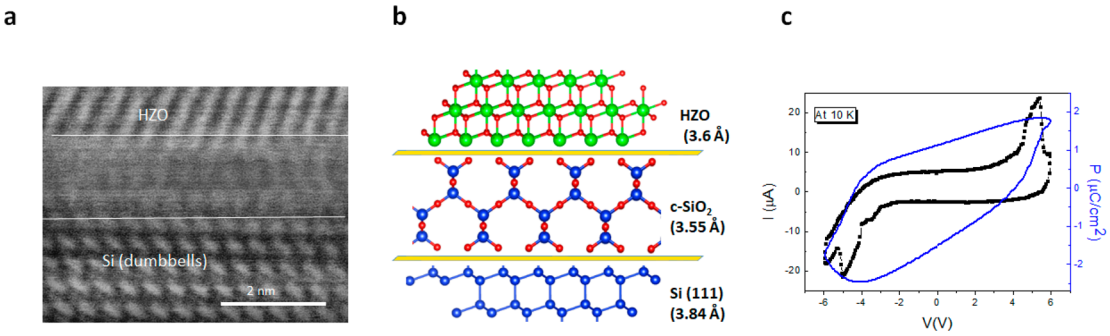

Figure 3. Interface structure and epitaxy on Si(111). (a) Bright-field (BF) cross-sectional STEM image with inverted contrast of the interface. BF mode provides better contrast for lighter elements, and thus, this mode of imaging is being reported. Clearly, we see 2−3 monolayers of interface with a different structure than both Si substrate and the HZO. This is a c-SiO_2 interface, with β-cristobalite or tridymite being the most likely phases. (b) Schematic of epitaxy on Si, with β-cristobalite at the interface. It provides the compressive strain necessary to stabilize the r-phase on HZO. (c) $I-V$, and corresponding $P-V$ loops obtained from the MIS capacitor structure of TiN−HZO (x = 0.7)-Si at 1000 Hz, and 10 K. Although quite leaky on the inversion side (negative voltage), we nevertheless see switching peaks in the $I-V$ curves. P_s is quite low, since the majority of the film is in a nonpolar monoclinic phase. However, this is a proof-of-concept that the r-phase is indeed polar.

Figures S1d and S2 for error estimation from $\theta-2\theta$ scans that can occur through slight misalignment and inhomogeneous strain). Such a 3:1 degeneracy in peak positions or $d_{\{111\}}$ is consistent with the low-volume phase having a rhombohedral symmetry, a phase which was recently discovered on films grown epitaxially on STO substrates.[39] In other words $(11\bar{1})$, $(1\bar{1}1)$, and $(\bar{1}11)$ have the same d-spacing, which is smaller than the (111) d-spacing. In orthorhombic, tetragonal, or cubic phases, all the four {111}s have the same d-spacing, whereas in a monoclinic phase there is a 2:2 degeneracy in these peak positions. The $d_{\{111\}}$ and $d_{\{1\bar{1}\bar{1}\}}$ can be calculated to be 2.96 (±0.01) Å and 2.95 (±0.01) Å, respectively, and this corresponds to a unit cell with $a = b = c \approx 5.11$ (±0.01) Å and rhombohedral angle (α) between 89.9° and 90°. This distortion is smaller than what was observed on the 10 nm HZO (x = 0.5) films grown on STO ($\alpha \sim 89.3°$).[39] Pole figures of the {002} planes obtained around $2\theta = 35°$ and corresponding $\theta-2\theta$ scans further confirm these lattice parameters (Figure S3).

HAADF-STEM images acquired on cross-sectional samples of films with x = 0.5 clearly show that the entire film is in the monoclinic (nonpolar) phase, consistent with the XRD data. EDS analysis shows a contiguous layer of amorphous a-SiO_x of ∼0.5 to 1 nm between Si and the HZO layer (Figure S4). This is a reformed oxide layer, a result of the backward reaction upon increasing the product concentration in the scavenging chemical reactions 1 and 2. With Zr concentration increased to x = 0.7, this a-SiO_x layer exists in some regions but is absent in some other regions (Figure 2c), a result of either the better scavenging properties of Zr ions compared to Hf ions or sluggish reduction kinetics of zirconia compared to hafnia. Very interestingly, upon analyzing the $d_{\{111\}}$ lattice parameters, we find that the film just above the regions with the a-SiO_x layer displays a monoclinic nonpolar phase ($d_{\{1\bar{1}\bar{1}\}} \approx 2.82$ Å, $d_{\{111\}} \approx 3.13$ Å), while the film directly in contact with Si substrate is in the low-volume phase (Figure 2c, zoomed in Figure 2d). HAADF-STEM multislice image (200 kV) simulations (Figure 2e) obtained from the rhombohedral ($R3$) phase (cross-sectional sample thickness of ∼20 nm), among all the other polymorphs, show the closest resemblance to our images. In particular, the alternating intensity of the cationic columns along the ⟨112⟩ direction is a distinct feature of the rhombohedral polar phases (both $R3$ and $R3m$), which can be seen in our experimental images (Figure 2d,f).

Interfacial Phase and Epitaxy. At the interface between Si and r-phase HZO, we observe at least two monolayers of crystalline phase, which is different from both the Si and HZO structures, as shown in the bright-field STEM image in Figure 3a (contrast digitally inverted). This is most likely a crystalline, tridymite or β-cristobalite, phase of SiO_2, which has been studied in detail at the Si/a-SiO_x interfaces and is well-known to induce epitaxy between Si and YSZ layers.[49,60−62] In Figure 3b, we propose a rough schematic for epitaxy, based on Figure 3a, assuming the lattice parameters of the β-cristobalite as the crystalline c-SiO_2 phase (in-plane ∼3.55 Å). Epitaxy of HZO (in-plane ∼3.6 Å) on c-SiO_2 thus provides initial compressive strain boundary conditions.

These results enable us to propose that the phase of the initial seed formed as a result of scavenging the native oxide is the low-volume r-phase. The compressive strain conditions stabilize the r-phase, quite similar to HZO films grown on STO.[39] However, regrowth of the amorphous oxide layer relaxes the strain, stabilizing the nonpolar m-phase.[49] Increasing the Zr content increases the efficiency of the native oxide scavenging, thus stabilizing a greater volume of the film in the r-phase.

Polar Nature of the r-Phase. Metal−insulator−semiconductor (MIS) capacitors were fabricated on these films with TiN (200 μm diameter) as the top-electrode. These were quite leaky especially in the inversion regime of operation. Cooling the devices to 10 K reduced the leakage, despite not completely avoiding it. On the films with x = 0.7, very weak polarization switching (evident from the $I-V$ loop) was observed with ΔP_s of ∼2 $\mu C/cm^2$ (Figure 3c), with devices tested at 1000 Hz. While the device optimization and rigorous electrical characterization is a subject of future work, these measurements demonstrate that the r-phase is indeed polar. About the weak ferroelectric switching, apart from the fact that these samples show a predominant fraction of nonpolar m-phase, it must also be noted that the rhombohedral angle in our samples is very close to 90°. First-principles calculations[39] show that, at these low distortions, the phase with $R3m$ symmetry has very low $P_s \sim 1$ $\mu C/cm^2$.

(0.3)HfO_2−(0.7)ZrO_2 on Si(100). *Textured {100} Films and Thickness Dependence.* On 5 nm thick films (Figure

DOI: 10.1021/acsaelm.9b00585
ACS Appl. Electron. Mater. 2019, 1, 2585−2593

4a,b), pole figures about $2\theta = 31°$ (approximately $d_{\{111\}}$ of HZO) show 4 {111} poles at $\chi \approx 53°$ separated in φ by 90°

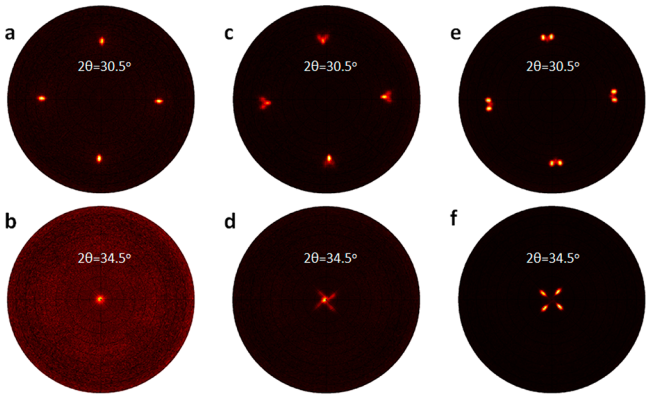

Figure 4. Texture measurements on HZO ($x = 0.7$) on Si(100) at different thicknesses. Pole figures obtained about $2\theta = 30.5°$ (corresponding to $d_{\{111\}}$) and about $2\theta = 34.5°$ (corresponding to $d_{\{100\}}$) on (a, b) 5 nm, (c, d) 10 nm, and (e, f) 20 nm HZO films grown on Si(100). (a, b) In 5 nm thick samples 4 {111} poles separated in φ by 90° are observed at $\chi \approx 53°$, and a {001} pole at $\chi \approx 0°$ clearly showing that the films are textured with ⟨001⟩ oriented out-of-plane. (c, d) In 10 nm thick samples, apart from the poles observed for 5 nm, there are some extra satellite {111} poles at $\chi \approx 58°$ forming a triangular pattern, and 4 {001} satellites centered around $\chi \approx 8°$ (spread = 8−10°) separated in φ by 90°. All these patterns can be mathematically explained through the coexistence of various monoclinic domains (each contributing to a different set of poles, see the Supporting Information). (e, f) What were just satellite spots in 10 nm samples become the main Bragg spots at 20 nm thickness.

(Figure 4a). Combined with the pole figure data at $2\theta = 34°$, which shows a {200}-pole at $\chi \approx 0°$ (Figure 4b), it is evident that these films are strongly textured with {100} planes parallel to the Si(100) surface. On 10 nm thick films (Figure 4c,d), along with all the poles observed for the 5 nm films, some extra satellites appear. Specifically, two satellites appear at $\chi \approx 58°$ for every intense {111} pole (at $\chi \approx 53°$) separated in φ by ∼7° (Figure 4c). About the intense center {100} pole, 4 different satellites appear centered at $\chi \approx 8°$ (with a spread of 8−10°) separated in φ by 90° (Figure 4d). These satellites hint of domains/grains where the {100} planes are misoriented with respect to the Si(100) surface. As the thickness of the film increases to 20 nm (Figure 4e,f), poles from these misoriented grains become the most intense, and the signal from the domains with {100}//Si(100) domains almost disappears.

Phase Coexistence, Domains, and Accordions. To further learn about the lattice parameters and global symmetries, $\theta-2\theta$ scans were performed across each of these pole figures. Here, we discuss the results from 10 nm films on Si(100), which include all the features of both the 5 nm and the 20 nm films. Around the {111} pole (zoomed in view in Figure 5a), when aligned perfectly either at $\chi \approx 53°$ (pixel 1 (black) in Figure 5a) or at the most intense spot of the satellites ($\chi \approx 58°$, gray pixels 6 and 7 in Figure 5a), $\theta-2\theta$ scans clearly show two distinct peaks centered at $2\theta = 28.5°$ and 31.5° (Figure 5b). This is a signature of the monoclinic phase, and its corresponding domain structure. In particular, the monoclinic domains that give rise to these Bragg spots (at χ and φ of the pixels 1, 6, and 7 in Figure 5b) correspond to two types of domains: those having the $a-b$ plane//Si(001) (dominating in

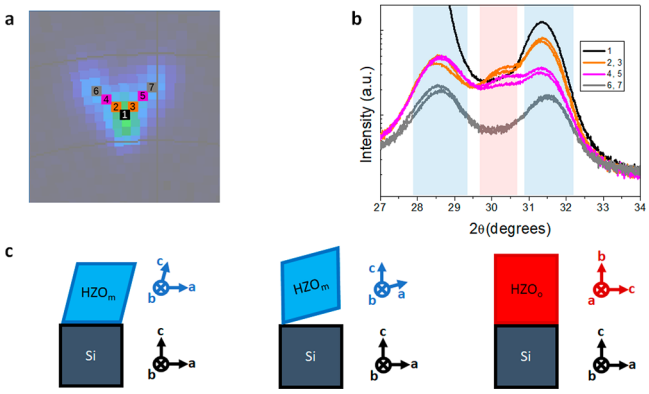

Figure 5. Phase coexistence and domains. (a) From Figure 4c (10 nm film thickness), one of the {111} poles and its corresponding satellites are zoomed in. The black pixel corresponds to $\chi = 53°$, where the {111} main pole is the most intense. The gray pixels correspond to $\chi = 58°$ where the satellites are the most intense. A progression from black to gray traverses through orange and magenta pixels, which correspond to purposeful misalignment ("well-aligned" conditions are obtained by maximizing the intensity, which would ignore information from orange and magenta pixels). (b) With the color coding scheme as described in part a, $\theta-2\theta$ scans were then performed at various χ values from the black pixel to the gray pixel. At the black or gray pixels, peaks corresponding to monoclinic {111} d-spacings are observed. In the orange and magenta pixels, however, a {111} peak corresponding to a low-volume phase appears at $2\theta \approx 30.2°$. (c) Various domains that correspond to the pole figures presented in Figure 4. The left one shows a monoclinic domain with $a-b$ plane of HZO//Si(100). This is very well-oriented growth observed at low film thicknesses (5 nm). The center panel shows a monoclinic domain with $a-b$ plane misaligned from the Si(100) surface. Negative and positive misorientations can give rise to an accordion-like zigzag pattern. The rightmost panel shows the domain from the low-volume phase (which can be shown to be orthorhombic from TEM results to follow).

thinner samples), and those with the $a-b$ plane a few degrees misoriented from Si (001) (in thicker samples), as sketched in Figure 5c. The separation in φ of the satellites is a result of domains with positive and negative misorientation. Rigorous proof of this model through a complete mathematical analysis of the pole figure analysis is provided in the Supporting Information (Figures S5 and S6 and related text).

When a $\theta-2\theta$ scan is performed at χ values in between the black and gray pixels (purposely "misaligned") in Figure 5a (pixels 2 and 3 (orange) and 4 and 5 (magenta)), we find the emergence of a third peak at $2\theta \approx 30.2°$ in addition to the two monoclinic {111} peaks (Figure 5b). This corresponds to a low-volume minor phase that coexists with the major bulk-monoclinic phase.

The overview cross-sectional HAADF-STEM image acquired along the [010] zone (Figure 6a) on the 10 nm thick film clearly shows an accordion-like domain morphology. Upon further zooming in (blue box in Figure 6a), we see that the domains that contribute to the zigzag pattern correspond very well to the monoclinic symmetry (HAADF-STEM simulation in Figure 6b). The monoclinic angle (β) varies between 95° and 99° across various domains. This variation is indeed reflected as the spread of the satellite spots about $\chi = 8°$ in the {001} pole figure (Figure 4d). The intersection of two domains with positive and negative misorientation (9° and −9° in Figure 6b) of the $a-b$ plane with Si (001) results in the accordion morphology, consistent with the satellite spots of the

DOI: 10.1021/acsaelm.9b00585
ACS Appl. Electron. Mater. 2019, 1, 2585−2593

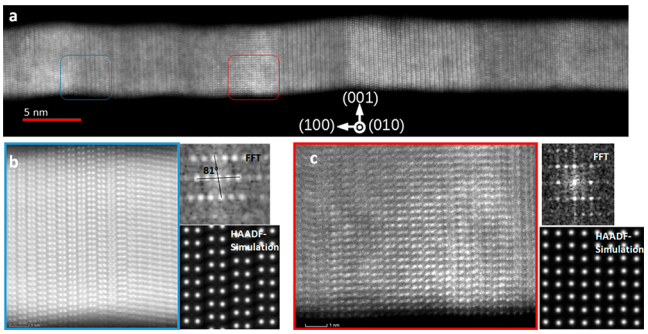

Figure 6. Monoclinic domains, orthorhombic domains, and accordions of HZO (x = 0.7, t = 10 nm) on Si(100). (a) Overview cross-sectional HAADF-STEM image along the [010] zone axis, of 10 nm thick HZO (x = 0.7), showing a clear accordion-like morphology. (b) Zoomed-in view of the region surrounded by a blue box in part a, showing the intersection of two domains. d-spacings estimated from the fast Fourier transform (FFT) obtained from the domain on the left confirm a monoclinic phase. Furthermore, the monoclinic angle (180°−β) can be directly read from the FFT to be ∼81° in this image. The a−b plane is misoriented with respect to the substrate (normal) by 9°. HAADF-STEM multislice image simulations of monoclinic phase, clearly matching our domain. If the domain on the left is positively misoriented with the substrate, the domain on the right is negatively misoriented, and their intersection gives rise to an accordion pattern. (c) Zoomed-in view of the region surrounded by the red box in part a. The d-spacing obtained from FFT clearly shows that this is in the o-phase ($d_{(002)}$ = 2.51 ± 0.02 Å, and $d_{(200)}$ = 2.57 ± 0.02 Å). HAADF-STEM image simulations match the real image (with zigzag arrangement of atomic columns along [001]). Simulations from different phases are compared in Figure S5. The polar axis, however, is the c-axis which is in-plane.

{111} poles in XRD analysis. The monoclinic domains corresponding to a−b plane//Si (001) are shown in the Supporting Information (Figure S7).

The region enclosed in red in Figure 6a, when zoomed and further analyzed, is consistent with our HAADF-STEM simulations from an orthorhombic crystal (Figure 6c), and not the other low-volume polymorphs (simulations of various polymorphs are compared in Figure S8). d-spacings for various crystallographic planes obtained from the HAADF-STEM image Fourier transform (Figure 6c) match very well with o-phase bulk lattice parameters.[63] In particular, $d_{(\text{in-plane})}$ = 2.51 ± 0.02 Å and $d_{(\text{out-of-plane})}$ = 2.57 ± 0.02 Å correspond to $d_{(002)}$ and $d_{(200)}$ for the o-phase, suggesting that the polar axis (c-axis in $Pca2_1$ symmetry) is in-plane. Thus, STEM analysis conclusively shows that, in addition to the various kinds of monoclinic domains (Figure 5c), a low-volume o-phase, the commonly occurring low-energy ferroelectric phase in polycrystalline thin films, is also present in these films.

Interface and Epitaxy. From EDS chemical maps (Figure 7a) and Wiener-filtered HAADF-STEM images (Figure 7b) at the interface between HZO and Si(100), it is quite clear that a contiguous layer of <1 nm regrown a-SiO_x exists. Furthermore, there also seems to be an interface c-SiO_2 (β-cristobalite, most likely) structure between Si(100) and the a-SiO_x, which enables epitaxy on Si(001).[49,60−62] The in-plane lattice parameter of β-cristobalite (5.03 Å) imposes a compressive strain on any polymorph of HZO. However, the regrowth of a-SiO_x relaxes this strain stabilizing most of the film in a bulk m-phase. Notably, the grains stabilizing in the o-phase also are interfaced with regrown a-SiO_x. This is unlike growth of HZO (x = 0.7) on Si(111), where there is a clear correlation

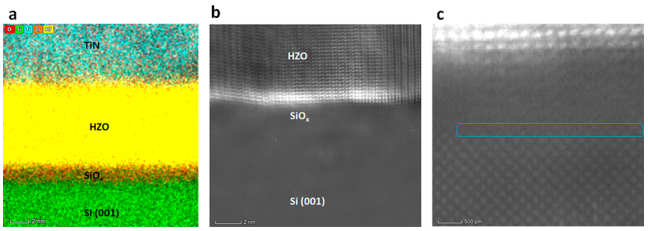

Figure 7. Interface and epitaxy on Si(100). (a, b) EDS chemical maps, and Wiener-filtered HAADF-STEM image clearly showing a regrown a-SiO_x layer of ∼1 nm between Si(100) and HZO (x = 0.7). (c) Zoomed-in view of Wiener-filtered image in part b. There is also an interfacial crystalline structure (boxed in blue) at the interface of Si and a-SiO_x, most likely belonging to c-SiO_2 in β-cristobalite phase. This enables an orientational relationship with the HZO layer.

between the existence of a low-volume phase, and the absence of regrown a-SiO_x on Si. Thus, it appears that the stabilization of o-phase is a result of the inhomogeneous strain fields originating at the intersection of various kinds of nanoscopic monoclinic domains that form the accordion, and not because of strain transfer from the substrate.

Polar r-Phase vs Polar o-Phase. Among all the polar polymorphs of hafnia, first-principles calculations suggest that the o-phase ($Pca2_1$) has the least energy (64 meV/f.u. with respect to the ground state).[39] The rhombohedral polymorphs ($R3m$, 158 meV/f.u.; and $R3$, 195 meV/f.u.), though more energetic, seem more favorable to obtain experimentally, under a combination of compressive strain and quite notably a (111) film orientation. Both the films grown on STO substrates by Wei et al.[39] and the films grown on Si(111) in the current work satisfy these conditions and, thus, exhibit a polar r-phase (and not the low-energy o-phase). These observations, however, are quite contradictory to the theoretical predictions of Liu and Hanrahan,[30] possibly owing to the absence of the r-phases in their calculations. It must also be noted that films grown in (001) orientation in this work show a preference for the o-phase, and not the r-phase. Such an orientation dependence of the obtained polar phase is very unique and deserves further investigation.

■ CONCLUSIONS

$(1 - x)HfO_2$−$(x)ZrO_2$ (HZO) with various compositions in the range 0.5< x < 0.85 was grown epitaxially on Si(111) and Si(100), without using buffer layers, using PLD. *In situ* scavenging of the native oxide using decomposition reactions plays a crucial role in achieving epitaxy directly on Si. On both of these substrates, an interfacial phase of c-SiO_2 (most likely β-cristobalite) has been found, and it offers initial compressive strain conditions for the growth of HZO. The regrowth of an amorphous a-SiO_x interlayer is a relaxation mechanism to release strain. On Si(111), the film on the top of the regions of regrown amorphous oxide relaxes to a bulk nonpolar monoclinic phase, and the film directly in connection with the c-SiO_2 is in the polar r-phase. The volume fraction of the r-phase increases, and the regrown a-SiO_x decreases with increasing Zr content, owing to better reactivity of Zr to participate in the a-SiO_x scavenging reaction (compared to Hf). Ferroelectric measurements show leaky and incipient, but clear, P−E hysteresis loops, evidence to the polar nature of the r-phase. On Si(100), the observed polar o-phase seems to be stabilized by inhomogeneous strains arising out of nanodomain coexistence of the surrounding m-phase. Finally, in addition to

DOI: 10.1021/acsaelm.9b00585
ACS Appl. Electron. Mater. 2019, 1, 2585−2593

strain and surface energy, there also appears to be an orientational dependence to the stabilization of polar phases (at least on Si); i.e., the r-phase is favored in (111) orientation, while the o-phase is preferred in (001).

■ ASSOCIATED CONTENT

Supporting Information

The Supporting Information is available free of charge at https://pubs.acs.org/doi/10.1021/acsaelm.9b00585.

Additional figures including HAADF-STEM images, pole figures, fitting procedure, error analysis, $\theta-2\theta$ scans, peak positions, EDS elemental maps, and a fast Fourier transform (PDF)

■ AUTHOR INFORMATION

Corresponding Authors

*E-mail: p.nukala@rug.nl.
*E-mail: b.noheda@rug.nl.

ORCID

Beatriz Noheda: 0000-0001-8456-2286

Author Contributions

‖P.N. and J.A.-L. contributed equally.

Notes

The authors declare no competing financial interest.

■ ACKNOWLEDGMENTS

P.N. acknowledges the funding received from European Union's Horizon 2020 research and innovation programme under Marie Sklodowska-Curie grant Agreement 794954 (Project name: FERHAZ). J.A.-L. and B.N. acknowledge the funding from NWO's TOP-PUNT Grant 718.016002. Y.W. and B.N. acknowledge the China Scholarship Council. L.Y. and B.D. acknowledge a public grant overseen by the French National Research Agency (ANR) as a part of the "Investissements d'Avenir" program (Grant ANR-10-EQPX-37, EquipEx MATMECA) and through ANR-17-CE24-0032/EXPAND.

■ REFERENCES

(1) Schröder, U., Hwang, C. S., Funakubo, H., Eds. *Ferroelectricity in Doped Hafnium Oxide*, 1st ed.; Woodhead Publishing, 2019.

(2) Böscke, T. S.; Müller, J.; Bräuhaus, D.; Schröder, U.; Böttger, U. Ferroelectricity in Hafnium Oxide Thin Films. *Appl. Phys. Lett.* **2011**, *99*, 102903.

(3) Park, M. H.; Lee, Y. H.; Mikolajick, T.; Schroeder, U.; Hwang, C. S. Review and Perspective on Ferroelectric HfO_2-Based Thin Films for Memory Applications. *MRS Commun.* **2018**, *8*, 795.

(4) Polakowski, P.; Riedel, S.; Weinreich, W.; Rudolf, M.; Sundqvist, J.; Seidel, K.; Muller, J. Ferroelectric Deep Trench Capacitors Based on Al:HfO_2 for 3D Nonvolatile Memory Applications. *2014 IEEE 6th International Memory Workshop, IMW 2014* **2014**, 1.

(5) Pešić, M.; Hoffmann, M.; Richter, C.; Mikolajick, T.; Schroeder, U. Nonvolatile Random Access Memory and Energy Storage Based on Antiferroelectric Like Hysteresis in ZrO_2. *Adv. Funct. Mater.* **2016**, *26*, 7486.

(6) Mulaosmanovic, H.; Ocker, J.; Muller, S.; Noack, M.; Muller, J.; Polakowski, P.; Mikolajick, T.; Slesazeck, S. Novel Ferroelectric FET Based Synapse for Neuromorphic Systems. *Digest of Technical Papers - Symposium on VLSI Technology* **2017**, T176.

(7) Müller, J.; Yurchuk, E.; Schlösser, T.; Paul, J.; Hoffmann, R.; Müller, S.; Martin, D.; Slesazeck, S.; Polakowski, P.; Sundqvist, J.; Czernohorsky, M.; Seidel, K.; Kücher, P.; Bosche, R.; Trentzsch, M.; Gebauer, K.; Schroeder, U.; Mikolajick, T. Ferroelectricity in HfO_2 Enables Nonvolatile Data Storage in 28 Nm HKMG. *Digest of Technical Papers - Symposium on VLSI Technology* **2012**, 25.

(8) Muller, J.; Boscke, T. S.; Muller, S.; Yurchuk, E.; Polakowski, P.; Paul, J.; Martin, D.; Schenk, T.; Khullar, K.; Kersch, A.; Weinreich, W.; Reidel, S.; Kumar, A.; Arruda, T. M.; Kalinin, S. V.; Schosser, T.; Boschke, R.; van Bentum, R.; Schroeder, U.; Mikolajic, T. Ferroelectric Hafnium Oxide: A CMOS-Compatible and Highly Scalable Approach to Future Ferroelectric Memories. *Technical Digest - International Electron Devices Meeting, IEDM* **2013**, 10-8-1.

(9) Wei, Y.; Matzen, S.; Agnus, G.; Salverda, M.; Nukala, P.; Chen, Q.; Ye, J.; Lecoeur, P.; Noheda, B. Magnetic Tunnel Junctions Based on Ferroelectric $Hf_{0.5}Zr_{0.5}O_2$ Tunnel Barriers. 2019, arXiV:1902.08021. arXiv preprint archive. https://arxiv.org/abs/1902.08021.

(10) Fan, C. C.; Cheng, C. H.; Tu, C. Y.; Liu, C.; Chen, W. H.; Chang, T. J.; Chang, C. Y. Achieving High-Scalability Negative Capacitance FETs with Uniform Sub-35 MV/Dec Switch Using Dopant-Free Hafnium Oxide and Gate Strain. *Digest of Technical Papers - Symposium on VLSI Technology* **2018**, 139.

(11) Dragoman, M.; Modreanu, M.; Povey, I. M.; Iordanescu, S.; Aldrigo, M.; Romanitan, C.; Vasilache, D.; Dinescu, A.; Dragoman, D. Very Large Phase Shift of Microwave Signals in a 6 nm $Hf_xZr_{1-x}O_2$ ferroelectric at ± 3 V. *Nanotechnology* **2017**, *28*, 38LT04.

(12) Müller, J.; Böscke, T. S.; Bräuhaus, D.; Schröder, U.; Böttger, U.; Sundqvist, J.; Kcher, P.; Mikolajick, T.; Frey, L. Ferroelectric $Zr_{0.5}Hf_{0.5}O_2$ Thin Films for Nonvolatile Memory Applications. *Appl. Phys. Lett.* **2011**, *99*, 112901.

(13) Park, M. H.; Lee, Y. H.; Kim, H. J.; Kim, Y. J.; Moon, T.; Kim, K. Do; Hyun, S. D.; Hwang, C. S. Morphotropic Phase Boundary of $Hf_{1-x}Zr_xO_2$ Thin Films for Dynamic Random Access Memories. *ACS Appl. Mater. Interfaces* **2018**, *10*, 42666.

(14) Sang, X.; Grimley, E. D.; Schenk, T.; Schroeder, U.; Lebeau, J. M. On the Structural Origins of Ferroelectricity in HfO_2 Thin Films. *Appl. Phys. Lett.* **2015**, *106*, 162905.

(15) Florent, K.; Lavizzari, S.; Popovici, M.; Di Piazza, L.; Celano, U.; Groeseneken, G.; Van Houdt, J. Understanding Ferroelectric Al:HfO_2 thin Films with Si-Based Electrodes for 3D Applications. *J. Appl. Phys.* **2017**, *121*, 204103.

(16) Shimizu, T.; Katayama, K.; Kiguchi, T.; Akama, A.; Konno, T. J.; Funakubo, H. Growth of Epitaxial Orthorhombic $YO_{1.5}$-Substituted HfO_2 Thin Film. *Appl. Phys. Lett.* **2015**, *107*, 032910.

(17) Schroeder, U.; Yurchuk, E.; Müller, J.; Martin, D.; Schenk, T.; Polakowski, P.; Adelmann, C.; Popovici, M. I.; Kalinin, S. V.; Mikolajick, T. Impact of Different Dopants on the Switching Properties of Ferroelectric Hafnium Oxide. *Jpn. J. Appl. Phys.* **2014**, *53*, 08LE02.

(18) Starschich, S.; Griesche, D.; Schneller, T.; Böttger, U. Chemical Solution Deposition of Ferroelectric Hafnium Oxide for Future Lead Free Ferroelectric Devices. *ECS J. Solid State Sci. Technol.* **2015**, *4*, P419.

(19) Sharma, Y.; Barrionuevo, D.; Agarwal, R.; Pavunny, S. P.; Katiyar, R. S. Ferroelectricity in Rare-Earth Modified Hafnia Thin Films Deposited by Sequential Pulsed Laser Deposition. *ECS Solid State Lett.* **2015**, *4*, N13.

(20) Grimley, E. D.; Schenk, T.; Sang, X.; Pešić, M.; Schroeder, U.; Mikolajick, T.; LeBeau, J. M. Structural Changes Underlying Field-Cycling Phenomena in Ferroelectric HfO_2 Thin Films. *Adv. Electron. Mater.* **2016**, *2*, 1600173.

(21) Lyu, J.; Fina, I.; Solanas, R.; Fontcuberta, J.; Sánchez, F. Robust Ferroelectricity in Epitaxial $Hf_{1/2}Zr_{1/2}O_2$ Thin Films. *Appl. Phys. Lett.* **2018**, *113*, 082902.

(22) Hoffmann, M.; Schroeder, U.; Schenk, T.; Shimizu, T.; Funakubo, H.; Sakata, O.; Pohl, D.; Drescher, M.; Adelmann, C.; Materlik, R.; Kersch, A.; Mikolajic, T. Stabilizing the Ferroelectric Phase in Doped Hafnium Oxide. *J. Appl. Phys.* **2015**, *118*, 072006.

(23) Barabash, S. V. Prediction of New Metastable HfO_2 phases: Toward Understanding Ferro- and Antiferroelectric Films. *J. Comput. Electron.* **2017**, *16*, 1227.

DOI: 10.1021/acsaelm.9b00585
ACS Appl. Electron. Mater. 2019, 1, 2585−2593

(24) Lyu, J.; Fina, I.; Solanas, R.; Fontcuberta, J.; Sánchez, F. Growth Window of Ferroelectric Epitaxial $Hf_{0.5}Zr_{0.5}O_2$ Thin Films. *ACS Appl. Electron. Mater.* **2019**, *1* (2), 220−228.
(25) Zacharaki, C.; Tsipas, P.; Chaitoglou, S.; Fragkos, S.; Axiotis, M.; Lagoyiannis, A.; Negrea, R.; Pintilie, L.; Dimoulas, A. Very Large Remanent Polarization in Ferroelectric $Hf_{1-x}Zr_xO_2$ Grown on Ge Substrates by Plasma Assisted Atomic Oxygen Deposition. *Appl. Phys. Lett.* **2019**, *114*, 112901.
(26) Luo, Q.; Ma, H.; Su, H.; Xue, K.-H.; Cao, R.; Gao, Z.; Yu, J.; Gong, T.; Xu, X.; Yin, J.; Peng, Y.; Lu, T.; Danian, D.; Shibing, L.; Qi, L.; Xiang-Shui, M.; Hangbing, L.; Ming, L. Composition-Dependent Ferroelectric Properties in Sputtered $Hf_xZr_{1-x}O_2$ Thin Films. *IEEE Electron Device Lett.* **2019**, *40* (4), 570−573.
(27) Katayama, K.; Shimizu, T.; Sakata, O.; Shiraishi, T.; Nakamura, S.; Kiguchi, T.; Akama, A.; Konno, T. J.; Uchida, H.; Funakubo, H. Orientation Control and Domain Structure Analysis of {100}-Oriented Epitaxial Ferroelectric Orthorhombic HfO_2-Based Thin Films. *J. Appl. Phys.* **2016**, *119* (13), 134101.
(28) Park, M. H.; Kim, H. J.; Kim, Y. J.; Moon, T.; Hwang, C. S. The Effects of Crystallographic Orientation and Strain of Thin $Hf_{0.5}Zr_{0.5}O_2$ film on Its Ferroelectricity. *Appl. Phys. Lett.* **2014**, *104*, 072901.
(29) Bouaziz, J.; Romeo, P. R.; Baboux, N.; Vilquin, B. Characterization of Ferroelectric Hafnium/Zirconium Oxide Solid Solutions Deposited by Reactive Magnetron Sputtering. *J. Vac. Sci. Technol., B: Nanotechnol. Microelectron.: Mater., Process., Meas., Phenom.* **2019**, *37*, 021203.
(30) Liu, S.; Hanrahan, B. M. Effects of Growth Orientations and Epitaxial Strains on Phase Stability of HfO_2 Thin Films. *Phys. Rev. Mater.* **2019**, *3*, 054404.
(31) Shimizu, T.; Katayama, K.; Kiguchi, T.; Akama, A.; Konno, T. J.; Sakata, O.; Funakubo, H. The Demonstration of Significant Ferroelectricity in Epitaxial Y-Doped HfO_2 Film. *Sci. Rep.* **2016**, *6*, 32931.
(32) Müller, J.; Böscke, T. S.; Schröder, U.; Mueller, S.; Bräuhaus, D.; Böttger, U.; Frey, L.; Mikolajick, T. Ferroelectricity in Simple Binary Alloys of ZrO_2 and HfO_2. *Nano Lett.* **2012**, *12*, 4318.
(33) Schenk, T.; Hoffmann, M.; Ocker, J.; Pešić, M.; Mikolajick, T.; Schroeder, U. Complex Internal Bias Fields in Ferroelectric Hafnium Oxide. *ACS Appl. Mater. Interfaces* **2015**, *7*, 20224.
(34) Chouprik, A.; Zakharchenko, S.; Spiridonov, M.; Zarubin, S.; Chernikova, A.; Kirtaev, R.; Buragohain, P.; Gruverman, A.; Zenkevich, A.; Negrov, D. Ferroelectricity in $Hf_{0.5}Zr_{0.5}O_2$ Thin Films: A Microscopic Study of the Polarization Switching Phenomenon and Field-Induced Phase Transformations. *ACS Appl. Mater. Interfaces* **2018**, *10*, 8818.
(35) Li, P.; Chen, I. W.; Penner-Hahn, J. E. X-Ray-Absorption Studies of Zirconia Polymorphs. I. Characteristic Local Structures. *Phys. Rev. B: Condens. Matter Mater. Phys.* **1993**, *48*, 10063.
(36) Howard, C. J.; Kisi, E. H.; Roberts, R. B.; Hill, R. J. Neutron Diffraction Studies of Phase Transformations between Tetragonal and Orthorhombic Zirconia in Magnesia-Partially-Stabilized Zirconia. *J. Am. Ceram. Soc.* **1990**, *73*, 2828.
(37) Adams, D. M.; Leonard, S.; Russell, D. R.; Cernik, R. J. X-Ray Diffraction Study of Hafnia under High Pressure Using Synchrotron Radiation. *J. Phys. Chem. Solids* **1991**, *52*, 1181.
(38) Sharma, G.; Ushakov, S. V.; Navrotsky, A. Size Driven Thermodynamic Crossovers in Phase Stability in Zirconia and Hafnia. *J. Am. Ceram. Soc.* **2018**, *101*, 31.
(39) Wei, Y.; Nukala, P.; Salverda, M.; Matzen, S.; Zhao, H. J.; Momand, J.; Everhardt, A. S.; Agnus, G.; Blake, G. R.; Lecoeur, P.; Kooi, B. J.; Íñiguez, J.; Dkhil, B.; Noheda, B. A Rhombohedral Ferroelectric Phase in Epitaxially Strained $Hf_{0.5}Zr_{0.5}O_2$ Thin Films. *Nat. Mater.* **2018**, *17*, 1095.
(40) Lyu, J.; Fina, I.; Bachelet, R.; Saint-Girons, G.; Estandia, S.; Gazquez, J.; Fontcuberta, J.; Sanchez, F. Enhanced Ferroelectricity in Epitaxial $Hf_{0.5}Zr_{0.5}O_2$ Thin Films Integrated with Si(001) Using $SrTiO_3$ Templates. *Appl. Phys. Lett.* **2019**, *114*, 222901.
(41) Yoong, H. Y.; Wu, H.; Zhao, J.; Wang, H.; Guo, R.; Xiao, J.; Zhang, B.; Yang, P.; Pennycook, S. J.; Deng, N.; Yan, X.; Chen, J. Epitaxial Ferroelectric $Hf_{0.5}Zr_{0.5}O_2$ Thin Films and Their Implementations in Memristors for Brain-Inspired Computing. *Adv. Funct. Mater.* **2018**, *50*, 1806037.
(42) Lyu, J.; Fina, I.; Fontcuberta, J.; Sánchez, F. Epitaxial Integration on Si(001) of Ferroelectric $Hf_{0.5}Zr_{0.5}O_2$ Capacitors with High Retention and Endurance. *ACS Appl. Mater. Interfaces* **2019**, *11*, 6224.
(43) Moya, J. S.; Moreno, R.; Requena, J.; Soria, J. Black Color in Partially Stabilized Zirconia. *J. Am. Ceram. Soc.* **1988**, *71*, C479.
(44) Sharath, S. U.; Vogel, S.; Molina-Luna, L.; Hildebrandt, E.; Wenger, C.; Kurian, J.; Duerrschnabel, M.; Niermann, T.; Niu, G.; Calka, P.; Lehman, M.; Kleebe, H.-J.; Schroeder, T.; Alff, L. Control of Switching Modes and Conductance Quantization in Oxygen Engineered HfOx Based Memristive Devices. *Adv. Funct. Mater.* **2017**, *27*, 1700432.
(45) Materlik, R.; Kunneth, C.; Kersch, A. The Origin of Ferroelectricity in $Hf_{1-x}Zr_xO_2$: A Computational Investigation and a Surface Energy Model. *J. Appl. Phys.* **2015**, *117*, 134109.
(46) Batra, R.; Huan, T. D.; Jones, J. L.; Rossetti, G.; Ramprasad, R. Factors Favoring Ferroelectricity in Hafnia: A First-Principles Computational Study. *J. Phys. Chem. C* **2017**, *121*, 4139.
(47) Mulder, M. *Epitaxial Hafnium Zirconate on GaN by Pulsed Laser Deposition*; University of Twente, 2019.
(48) Wakiya, N.; Yoshida, M.; Al, E. *Grain Boundary Engineering in Ceramics*; American Ceramic Society, 2000.
(49) Ishigaki, H.; Yamada, T.; Wakiya, N.; Shinozaki, K.; Mizutani, N. Effect of the Thickness of SiO_2 under Layer on the Initial Stage of Epitaxial Growth Process of Yttria-Stabilized Zirconia (YSZ) Thin Film Deposited on Si(001) Substrate. *Nippon Seramikkusu Kyokai Gakujutsu Ronbunshi* **2001**, *109*, 766.
(50) Wang, S. J.; Ong, C. K. Epitaxial Y-Stabilized ZrO_2 films on Silicon: Dynamic Growth Process and Interface Structure. *Appl. Phys. Lett.* **2002**, *80*, 2541.
(51) Lubig, A.; Buchal, C.; Guggi, D.; Jia, C. L.; Stritzker, B. Epitaxial Growth of Monoclinic and Cubic ZrO_2 on Si(100) without Prior Removal of the Native SiO_2. *Thin Solid Films* **1992**, *217*, 125.
(52) Bardal, A.; Matthée, T.; Wecker, J.; Samwer, K. Initial Stages of Epitaxial Growth of Y-stabilized ZrO_2 Thin Films on A-SiO_x/Si(001) Substrates. *J. Appl. Phys.* **1994**, *75* (6), 2902−2910.
(53) Dubbink, D.; Koster, G.; Rijnders, G. Growth Mechanism of Epitaxial YSZ on Si by Pulsed Laser Deposition. *Sci. Rep.* **2018**, *8* (1), 5774.
(54) Hirai, T.; Teramoto, K.; Nagashima, K.; Koike, H.; Matsuno, S.; Tanimoto, S.; Tarui, Y. Crystal and Electrical Characterizations of Oriented Yttria-Stabilized Zirconia Buffer Layer for the Metal/Ferroelectric/Insulator/Semiconductor Field-Effect Transistor. *Jpn. J. Appl. Phys.* **1996**, *35* (1-7), 4016−4020.
(55) Fenner, D. B.; Viano, A. M.; Fork, D. K.; Connell, G. A. N.; Boyce, J. B.; Ponce, F. A.; Tramontana, J. C. Reactions at the Interfaces of Thin Films of Y-Ba-Cu- and Zr-oxides with Si Substrates. *J. Appl. Phys.* **1991**, *69* (4), 2176−2182.
(56) Gsell, S.; Fischer, M.; Bauer, T.; Schreck, M.; Stritzker, B. Yttria-Stabilized Zirconia Films of Different Composition as Buffer Layers for the Deposition of Epitaxial Diamond/Ir Layers on Si(001). *Diamond Relat. Mater.* **2006**, *15*, 479.
(57) Ockenfuß, G.; Baudenbacher, F.; Prusseit-Elffroth, W.; Hirata, K.; Berberich, P.; Kinder, H. Preparation and Growth of YSZ Buffer Layers and $YBa_2Cu_3O_7$ - Films on Silicon (100). *Phys. C* **1991**, *180* (1), 30−33.
(58) Myoren, H.; Nishiyama, Y.; Fukumoto, H.; Nasu, H.; Osaka, Y. As-Grown Preparation of Superconducting Epitaxial $Ba_2YCu_3O_x$ Thin Films Sputtered on Epitaxially Grown ZrO2/Si(100). *Jpn. J. Appl. Phys.* **1989**, *28* (1-3), 351−355.
(59) Bunt, P.; Varhue, W. J.; Adams, E.; Mongeon, S. Initial Stages of Growth of Heteroepitaxial Yttria-Stabilized Zirconia Films on Silicon Substrates. *J. Electrochem. Soc.* **2000**, *147*, 4541.
(60) Ourmazd, A.; Taylor, D. W.; Rentschler, J. A.; Bevk, J. Si→SiO_2 Transformation: Interfacial Structure and Mechanism. *Phys. Rev. Lett.* **1987**, *59* (2), 213−216.

DOI: 10.1021/acsaelm.9b00585
ACS Appl. Electron. Mater. 2019, 1, 2585−2593

(61) Ohdomari, I.; Akatsu, H.; Yamakoshi, Y.; Kishimoto, K. The Structural Models of the Si/SiO_2 Interface. *J. Non-Cryst. Solids* **1987**, *89* (1), 239−248.
(62) Hane, M.; Miyamoto, Y.; Oshiyama, A. Atomic and Electronic Structures of an Interface between Silicon and β-Cristobalite. *Phys. Rev. B: Condens. Matter Mater. Phys.* **1990**, *41* (18), 12637−12640.
(63) Ohtaka, O.; Yamanaka, T.; Kume, S.; Hara, N.; Asano, H.; Izumi, F. Structural Analysis of Orthorhombic Hafnia by Neutron Powder Diffraction. *J. Am. Ceram. Soc.* **1995**, *78* (1), 233−237.

DOI: 10.1021/acsaelm.9b00585
ACS Appl. Electron. Mater. 2019, 1, 2585−2593